Accepted Manuscript

Hot deformation mechanisms and microstructure evolution of SiCp/2014Al composite

Zhiye Huang, Xingxing Zhang, Bolyu Xiao, Zongyi Ma

PII: S0925-8388(17)32052-2

DOI: 10.1016/j.jallcom.2017.06.065

Reference: JALCOM 42133

To appear in: *Journal of Alloys and Compounds*

Received Date: 22 March 2017

Revised Date: 20 May 2017

Accepted Date: 5 June 2017

Please cite this article as: Z. Huang, X. Zhang, B. Xiao, Z. Ma, Hot deformation mechanisms and microstructure evolution of SiCp/2014Al composite, *Journal of Alloys and Compounds* (2017), doi: 10.1016/j.jallcom.2017.06.065.

Hot deformation mechanisms and microstructure evolution of SiCp/2014Al composite

Zhiye Huang [a,b], Xingxing Zhang [a], Bolyu Xiao [a,*], Zongyi Ma [a]

[a] Shenyang National Laboratory for Materials Science, Institute of Metal Research, Chinese Academy of Sciences, 72 Wenhua Road, Shenyang 110016, China

[b] School of Materials Science and Engineering, University of Science and Technology of China, Hefei 230001, China

Abstract:

Hot deformation behavior of a stir cast and hot extruded 14 vol.% SiCp/2014Al composite was studied at temperatures from 355 to 495 ºC and strain rates from 0.001 to 1 s^{-1}, including microstructure evolution and damage formation. Stress-strain rate fitting was optimized to construct accurate processing maps based on modified dynamic materials model (MDMM). In addition, the strain rate sensitivity maps were plotted, indicating more significant effect of temperature on deformation mechanism than strain rate. The dissipation efficiency versus temperature curves indicated: (i) a transition from dynamic recovery (DRV) to dynamic recrystallization (DRX) at 400 ºC; (ii) occurrence of dynamic grain growth (DGG) at 400-440 ºC; (iii) existence of equicohesive point (T_{eq}) of 450 ºC (~0.8 T_m) above which grain boundaries weakened and contributed to plastic deformation. The particular fluctuation of temperature sensitivity at 440 ºC was caused by an abnormal grain growth.

Keywords: Metal matrix composites; Hot deformation; Processing map; Dynamic recovery; Dynamic recrystallization

*Corresponding author. Tel.: +86-24-83978630, Fax: +86-24-23971749, E-mail address:, blxiao@imr.ac.cn (B.L. Xiao).

1. Introduction

Particulate reinforced aluminum matrix composites (PRAMCs) have found wide applications in aerospace, electronic and automotive industries over the past decades [1-4]. Among of them, silicon carbide particulate reinforced aluminum (SiCp/Al) composites with relatively low cost generally offers improved wear resistance, higher elastic modulus, lower coefficient of thermal expansion (CTE) and dimensional stability compared to unreinforced matrix alloys. Although the SiCp/Al composites can be subjected to conventional hot working such as forging, rolling, and extrusion [5-8], the addition of SiCp reinforcements increases the resistance to plastic deformation and then brings the risk of damage during hot working. Furthermore, the complicated microstructures of the SiCp/Al composites also restrict accurate identification of hot deformation mechanisms, leading to low controllability of microstructures.

The dynamic materials model (DMM) [9] provides an useful tool for studying the deformation behavior of the SiCp/Al composites. Microstructure evolution can be predicted by analyses of the power dissipation efficiency combined with essential microstructure observations [10-17]. In the DMM [9] the stress-strain rate (σ-$\dot{\varepsilon}$) relation is presumed to satisfy the power law in any instance. However, most materials cannot actually follow this assumption. Subsequently, Murty et al. [18] modified the DMM to reduce the deviation by the integral of fitted stress versus strain rate curves rather than the power law assumption. Nevertheless, details of the fitting method for stress versus strain data were not discussed in the related references [12,

13, 18, 19]. Because of the uncertain integration method and the complicated solution procedure, for various alloys and composites the processing maps so far were mostly established by the DMM [20-27] instead of the modified DMM (MDMM) with higher accuracy.

In fact, deformation mechanisms are related to many factors including dislocation movement, grain boundary migration, concentration of point defects, phase transition, etc. Variation of these factors could be further reflected by temperature dependence of flow stress. During hot working, the temperature sensitivity of flow stress (*s* value) was generally used to evaluate the instability criteria derived from Liapunov function [14, 19, 28-30] and rarely was employed to explain the transformation of hot deformation mechanism. Taking the correlation of *s* value and deformation mechanism into account can overcome the inadequacy characterized only by the dissipation efficiency.

The physical meaning of the instability criterion in the DMM is that if the system is unable to generate entropy at a rate to match the imposed rate, the plastic flow of materials will localize, which would cause the flow instability [31]. Typical metallurgical features of instability during hot working include flow localization, adiabatic shear bands, kink bands, intense deformation bands, dynamic strain aging etc. [32]. The instability generally refers to the severe local deformation in the view of solid mechanics, whereas the concept of damage usually implies the unrecoverable breaking of macro or micro-structures. During hot deformation, the damage processes involve ductile fracture at hard particles, wedge cracking, intercrystalline cracking,

cracking along prior particle boundaries, etc. [31].

In the studies of hot workability for Al or Mg matrix composites [23, 24, 33, 34], the instable region of DMM commonly was used to identify the unsafe processing parameters. With respect to the distinction between the concepts of instability and damage, the observation of single deformed sample within instability parameter (from DMM) [10, 11, 35] instead of the all samples is not completely reliable for conforming damage condition.

This study aims to rationalize the variation of performance parameters in a stir cast 14 vol.% SiCp/2014Al composite, including temperature sensitivity, strain rate sensitivity and power dissipation efficiency with microstructure evolution based on the MDMM. Microstructure evolution was investigated throughout the whole cross-section of the samples after hot compression. The instability flowing behaviors were checked using all deformed samples. In addition, the evolution of internal damage in SiCp/Al composite was discussed.

2. Experimental details

A 14 vol.% SiCp/2014Al composite with a nominal SiC particle size of 20 μm was fabricated by stir casting and hot extrusion. The nominal chemical composition of 2014Al is Al-4.8Cu-0.6Mg-0.7Mn-0.7Fe-0.9Si [35], and preparation method of the composite was described in the references [36]. Details of the processing technique are considered to be proprietary by the manufacturer. Cylindrical specimens 8 mm in diameter and 12 mm in height were machined from the extruded bar with the axis of specimens parallel to the extrusion direction. The cylindrical surface of the specimens

was polished using 400 grit paper in order to observe cracks on the surface of the compressed specimens.

Isothermal compression test was conducted at temperatures of 355, 390, 425 and 495 ºC and strain rates of 0.001, 0.01, 0.1 and 1 s^{-1} on Gleeble-3800. Tantalum sheets were used to lubricate both end surfaces of the specimens. The specimens were compressed to a true strain of 0.9 at constant strain rates. After hot compression, the specimens were quenched into water to freeze the microstructure. The specimens for microstructural observation were mechanically polished, and etched using Keller's reagent. Microstructures were examined by stereo microscopy (SM; Zeiss Stemi 2000-C), light microscopy (OM; Zeiss Axiovert 200 MAT), scanning electron microscopy (SEM; FEI Quanta 600).

3. Results and discussion

3.1 Initial microstructure

Fig. 1 shows the microstructure of the as-received composite along the extrusion direction. The SiC particles were uniformly distributed and aligned into string-like arrays along the extrusion axis (Fig. 1a). The matrix (representing 2014Al alloy in this work) exhibited a fine-grained recrystallized microstructure due to extruding (Fig. 1b). The uniform equiaxed grains have an average size of ~2.5 μm which is rather close to the lower limit of subgrain size (~2 μm) of hot deformation [37]. The matrix consisted of Al-rich solid solution with other microstructural constituents. By means of SEM/EDS results (Fig. 1c), it can be identified that there exist two microstructural constituents in the composites, as shown in Fig. 1d. The phase with spheroid shape

marked "A" is $CuAl_2$, and the phase B is α-Al(Fe, Mn)Si with a polyhedral shape.

3.2 True stress-strain curve

Fig. 2 shows the typical compressive flow stress curves of the 14 vol.% SiCp/2014Al composite. In Fig. 2a, the flow stress increased gradually with increasing strain rate at 390 ºC. The same trend was found at the other temperatures. It is also seen in Fig. 2a that the curves exhibit an evident peak stress at initial deformation stage except for that at strain rate of 0.001 s^{-1}. This stress decrease after the peak is commonly related to the dislocation annihilation caused by dynamic recovery (DRV) or dynamic recrystallization (DRX) [38, 39]. The curve of 390 ºC and 0.001 s^{-1} yields at 16 MPa and exhibits a strain hardening. Compression at this condition could be thought to a creep process as reported in previous studies [40-44], in which dislocation climb and vacancy diffusion operated. The work hardening induced by creep deformation and the recovery softening reached an equilibrium, and then the hardening rate remained almost constant.

It can be seen in Fig. 2b that the flow stress curves at all temperature and moderate strain rate exhibit a yield peak. A lower yield point (denoted by dashed lines) appears after yield. At 355 and 390 ºC, the lower yield points are located at strain of ~0.06, while the points move to the strain of ~0.08 at 425, 460, and 495 ºC. The transition of the lower yield point can be attributed to variant of softening mechanisms such as DRV or DRX. In addition, the flow stress at 460 ºC and 0.1 s^{-1} is close to that at 425 ºC and 0.1 s^{-1}, which might also be related to the microstructure transition. These two distinctions among the flow curves at different temperatures will be interpreted in the

latter section of this paper.

3.3 Processing map theory

3.3.1 Modified dynamic materials model (MDMM)

The concept of dynamic materials model (DMM) was proposed by Prasad et al. [9]. According to the DMM, the instantaneous total power P can be divided into two complementary parts of dissipation power content G and co-content J . The G represents the power dissipated by plastic working, and the J is related to the metallurgical mechanisms. If the flow stress and strain rate obeyed power-law constitutive equation [9, 32], the J can be evaluated by

$$J = \int_0^{\sigma} \dot{\varepsilon} \cdot d\sigma = \left(\frac{m}{m+1} \sigma \dot{\varepsilon} \right)_{\varepsilon,T} \tag{1}$$

Under ideal conditions (m = 1), the J would reach the maximum $J_{\max}$, then the efficiency of power dissipation can be obtained by

$$\eta = J / J_{\max} = 2m/(m+1) \tag{2}$$

Kumar and Prasad [45, 46] combined the DMM with Ziegler's unstable condition under large plastic deformation [47] to propose an instability criterion

$$\xi(\dot{\varepsilon}) = \frac{\partial \ln[m/(m+1)]}{\partial \ln \dot{\varepsilon}} + m < 0 \tag{3}$$

The flow instabilities will occur when the instability parameter $\xi(\dot{\varepsilon})$ is negative.

The dissipation efficiency solved by Eq. (4) is valid only if the σ-$\dot{\varepsilon}$ curve obeys the power law relationship, whereas it cannot be completely satisfied for various alloy systems. Subsequently, Murty et al. [18] proposed a modified DMM. In the test strain rate range ($\geq \dot{\varepsilon}_{\min}$) G is evaluated by integrating the fitted curves of σ-$\dot{\varepsilon}$ experiment

data, then

$$G=\int_0^{\dot{\varepsilon}_{\min}}\sigma d\dot{\varepsilon}+\int_{\dot{\varepsilon}_{\min}}^{\dot{\varepsilon}}\sigma d\dot{\varepsilon}=\left(\frac{\sigma\dot{\varepsilon}}{m+1}\right)_{\dot{\varepsilon}=\dot{\varepsilon}_{\min}}+\int_{\dot{\varepsilon}_{\min}}^{\dot{\varepsilon}}\sigma d\dot{\varepsilon}\,. \tag{4}$$

Using the obtained G, the dissipation efficiency η can be calculated by

$$\eta=J/J_{\max}=\frac{J}{P/2}=2\left(1-\frac{G}{P}\right)_{\varepsilon,T}. \tag{5}$$

The instability criterion in the MDMM also derives from Ziegler's unstable condition

$$\xi'=\frac{2m}{\eta}-1<0. \tag{6}$$

3.3.2 Comparison with the curve-fitting methods for solving *G* value

The σ vs. $\dot{\varepsilon}$ relationships at 390 ºC and a true strain of 0.6 were fitted using various function, as shown in Fig. 3a. It can be seen that the power law and logarithm cubic spline curves are smoother than the others. In order to verify the deviation between the fitted curves and test data, hot compression tests were also conducted at 0.04 s^{-1} and 0.4 s^{-1}, respectively for 390 ºC. Comparing the deviations between the fitted curves and the verification points, it is observed that the logarithm cubic spline curve is more accurate than the power law curve.

The curves in Fig. 3b were the logarithmic data replotted from Fig. 3a. The direct cubic spline, cubic polynomial and linear interpolation curves obviously twist and deviate from the verification points. By contrast, the power law fitted curve has been transformed into a straight line with relatively higher deviation to verification points than the logarithm cubic spline curve. Therefore, the logarithm cubic spline is the most optimized method for fitting σ vs. $\dot{\varepsilon}$ curve. This indicates that the σ vs. $\dot{\varepsilon}$ relationship does not completely fall in the power law. Similar situation was also

observed in other metallic materials such as Al alloys, Al matrix composites (AMCs), Ti alloys and steels [48-51].

3.3.3 Processing maps

Power dissipation map and instability map were plotted based on the MDMM. Fig. 4 shows the processing maps at true strains of 0.3 and 0.8, corresponding to the primary stage of steady plastic flow and the terminal stage of hot compression, respectively. The grey areas denote the instability region ($\xi' < 0$), which is located at 450-495 ºC and 0.1-1 s^{-1}. The dissipation efficiencies at strains of 0.3 and 0.8 show some similarity in the overall distribution. The η value in both maps have two valley regions and one peak region:

(1) The first valley domain is located around 350-390 ºC and 0.001-1 s^{-1} in both maps;

(2) The second valley domain is located around 440-470 ºC and 0.001-0.01 s^{-1} in both maps;

(3) The peak domain is located around 460-495 ºC and 0.018-0.18 s^{-1} in the map with strain of 0.3, while the peak domain is located around 480-495 ºC and 0.001-0.1 s^{-1} in the map with strain of 0.8.

In addition, there exist slight discrepancies in the two maps of different strains. At strain of 0.3, the η value increases with temperature in the range of 390-440 ºC, whereas at strain of 0.8 the η contour is flat in the same temperature range. The peak domain of η value at the right bottom corner of the map shifts toward high temperature and low strain rate region as the strain increases from 0.3 to 0.8.

For PRAMCs [52-54], DRX generally occurs in the temperature and strain rate range of 400-450 ºC and 0.01-1 s^{-1}. The corresponding η value ranges from 21 to 30 (η, %). However, DRV usually dominates at the lower temperature of 300-400 ºC with η value ranging from 10 to 25. The peak value of η is commonly related to superplasticity [10].

3.4 Strain rate sensitivity and temperature sensitivity maps

3.4.1 Strain rate sensitivity map

Fig. 5 shows the strain rate sensitivity map at a true strain of 0.8, which is similar to the contour of dissipation efficiency map (Fig. 4b). The similar result was also reported in references [55, 56]. Two main domains are observed in Fig. 5. Domain I is located at the left half of the *m* value map in the temperature range of 355-440 ºC. The *m* value is lower and changes slightly with strain rate at a constant temperature, and also rises gradually as the temperature increases.

Domain II is located at the right bottom corner of the *m* value map, in the temperature range of 470-495 ºC and strain rate range of 0.001-0.1 s^{-1}. In this region, the *m* value rises abruptly as the temperature increases. At high temperatures (~0.8 T_m), diffusion-controlled plastic deformation such as dislocation climb, point defect diffusion and grain boundary sliding are dominant deformation mechanism. The strain rate has a significant influence on the deformation controlled by diffusion. Therefore, the *m* presents a high level at elevated temperature and low strain rate. The value of *m* is in the range from 0.1 to 0.2 at temperatures of 355-440 ºC and increases to 0.14-0.3 at temperatures above 440 ºC, yet a value of m>0.3 commonly delineates the

superplastic regime [57].

3.4.2 Temperature sensitivity map

The flow-stress dependence upon temperature is defined as a temperature sensitivity of flow stress *s*, which is determined as follows [30]:

$$s = \left[\frac{1}{T} \frac{\partial \ln \sigma}{\partial \left(1/T \right)} \right]_{\dot{\varepsilon},\varepsilon} \tag{9}$$

Where σ is flow stress (MPa), T absolute temperature (K).

Fig. 6 shows the temperature sensitivity map at true strains of 0.3 and 0.8. The contours of *s* are quite similar at the both strains. The *s* map can be divided into three temperature ranges as shown in Fig. 6b. In Range I (355-420 ºC) and III (460-495 ºC), the *s* value increases with decreasing strain rate. Especially in Range III, *s* value increases significantly with increasing temperature, and exhibits a peak in the region of 0.001-0.01 s^{-1} and 470-495 ºC. It signifies that flow stress is more sensitive to temperature at the lower strain rate and higher temperature conditions. Additionally, the *s* undergoes a particular lower level at temperature range of 420-460 ºC. It might be related to some microstructure transition. In fact, the *s* value in this temperature range has reached the flow instability condition ($s < 1$) suggested by Gegel et al. [28].

3.5 Microstructure verification

3.5.1 *s* dependence of microstructure

Fig. 7 shows the variation of *s* with temperature, which is produced based on the data in Fig. 6b. It is obvious that at 440 ºC all *s* curves present a valley that might indicate a metallurgical transformation. Fig. 8 shows the microstructure of the

compressed specimens at 425 ºC/0.01 s^{-1} and 460 ºC/0.01 s^{-1}. The deformed specimens were sectioned along the longitudinal direction (parallel to compression loading) for metallographic examination. In Fig. 8a, the grain boundary structure could not be identified by stereomicroscope at 425 ºC/0.01 s^{-1}, whereas at 460 ºC/0.01 s^{-1} abnormal grain growth (AGG) occurred. Furthermore, the grain shape after AGG is not uniform in the specimen interior, and it can be partitioned into four regions: I Hard-to-deform zone; II Shear deformation zone; III Compressive deformation zone; IV Lateral zone.

Fig. 8b illustrates the view field locations of the specimen longitudinal section. From massive examinations, it was seen that variation of microstructure with the compression parameters was distinct at shear deformation region rather than at compressive deformation region. Therefore, microstructure characterization was conducted mainly at the shear deformation region in this study.

After compressed at 425 ºC and 0.01 s^{-1}, the specimen exhibited typical DRX microstructure in the shear deformation zone, as shown in Fig. 8c. The uniform fine grains are aligned along the shear direction. The mean grain size of 3.6 μm is larger than the initial grain size (2.5 μm) of the as-received composite. The effect of deformation at temperatures above half absolute melting point leads to a grain growth, known as strain-induced or dynamic grain growth (DGG) [58, 59]. When the temperature increased to 460 ºC, some grains grew to around 100 μm (Fig. 8d). Only several small grains remained in the vicinity of particulate clusters denoted by the black arrows, as shown in Fig. 8e.

As shown in Fig. 9, the volume fraction of $CuAl_2$ constituents, particularly for the $CuAl_2$ with small size, in the matrix compressed at 425 ºC/0.01 s^{-1} is less than that at 460 ºC/0.01 s^{-1}. Generally, the dissolution temperature of $CuAl_2$ is above 500 ºC under solid solution condition [60], whereas the α-Al(Fe, Mn)Si cannot be dissolved by solution treatment. During hot deformation, the $CuAl_2$ partially re-dissolve at the lower temperature of ~460 ºC, because the large volume of lattice defects can offer the adequate passages for atom diffusion. The dissolution of $CuAl_2$ weakens the pinning effect on grain boundaries, which also promotes the AGG.

In Fig. 7, the curve of strain rate 1 s^{-1} appears flatter without a valley, whereas there still exists an increasing inflection of *s* value at 440 ºC. After compression at 425 ºC/1 s^{-1}, the microstructure exhibited fine equiaxed grains with a mean grain size of 3.1 μm (Fig. 10a), which is slightly larger than the initial grain size (2.5 μm), and due to the insufficient restoration the long grains were similar to those in the initial microstructure. At 460 ºC, AGG took place immediately after the specimen was heated to a temperature high enough to make grain boundaries sufficiently mobile, even at the high strain rate of 1 s^{-1} (Fig. 10b).

3.5.2 η dependence of microstructure

As shown in Fig. 4b, in the regime below 440 ºC, the η changes little with strain rate and the *m* presents a similar situation (Fig. 5). It implies that below 440 ºC, the dissipation efficiency and flow stress are not sensitive to the variation of strain rate. Therefore, in this temperature range the microstructural transition may be determined only by the temperature variation. Combining the variation of η curves (Fig. 11) with

the microstructure of corresponding specimens, three mechanisms of the microstructural evolution in the matrix may be determined during hot working:

(1) Temperature range of 350-400 ºC (η = 20-30, DRV)

Fig. 12a shows metallographic micrograph of the specimen deformed at 390 ºC and 0.001 s^{-1}. Some grains elongated along the direction of shear stress and a small number of grains were not clear. These characteristics are in agreement with the microstructures of DRV. The original high angle boundaries do not migrate significantly, and thus the grains would continue to change shape with deformation. Because the structures with higher dislocation density are difficult to etch especially in the AMCs, for the fine-grained PRAMCs fabricated by cast-plus-extruded route, the DRV microstructures have not been observed in the previous investigations [10, 11, 15, 17, 35, 61]. Wang et al. [35] only inferred the possibility of DRV by the shape of stress-strain curves.

Fig. 13a shows a TEM micrograph of the specimen deformed at 355 ºC and 1 s^{-1}. It can be seen that $CuAl_2$ phases adhere the interface of SiC, and many subgrains (SG) are situated at the vicinity of the SiC particle. The microscopic mechanism of DRV is related to some substructure evolutions, including the formation of low angle boundaries caused by dislocation climb, cross-slip and glide, and the movement of sub-boundaries driven by applied stress, etc. [62]. Because of the deformation incompatibility between the SiC particles and the matrix, dislocations readily accumulate near the particles. For the aluminum alloys with high stacking fault energy, dislocations tend to tangle and form the cell structures which further develop into

subgrains.

(2) Temperature range of 400-440 ºC (η = 26-32, DRX)

At 425 ºC, the metallographic micrographs of the specimens at different strain rates are shown in Fig. 8c, Fig. 10a, and Fig. 12b, respectively. The distinct boundaries imply a high proportion of high angle grain boundaries in the matrix. The equiaxed grains are aligned approximately parallel to the shear direction with evident microstructural features of DRX. Based on the discussion in section 3.5.1, it can be concluded that at temperature range of 400-440 ºC, DGG is the dominant mechanism of microstructural evolution. At 425 ºC, the average grain sizes for strain rates of 1.0, 0.01 and 0.001 s^{-1} are 3.1, 3.6 and 3.7 μm respectively, which increase as strain-rate declines. At high temperatures of above 350 ºC, when the grain size reaches a limit subgrain size (~2 μm), it does not decreases further with increasing strain due to DGG [37]. The original grain size of the as-received composite is ~2.5 μm that is approximately close to the limit subgrain size. Therefore, DRX can only take place in a manner of DGG in this temperature range.

Fig. 13b shows a TEM micrograph of the specimen deformed at 425 ºC and 1 s^{-1}. The $CuAl_2$ phases are located at the grain boundary. At this higher deformation temperature, dislocations and sub-structures around SiC particles can be consumed by DRX. Then, the recrystallized grains with uniform size formed near the SiC particle. Concerning the influence of reinforcements on the recrystallization, Humphreys [63] suggested that at lower temperature a deformation zone containing high dislocation density and large lattice misorientations exists in the matrix nearby particles, and this

can provide a large driving force and sites for particle stimulated nucleation (PSN) of recrystallization on subsequent annealing. However, during deformation at elevated temperatures, dislocations may be able to climb around the particles, so no accumulation of dislocations will occur. Hence, the PSN of recrystallization will not occur [64].

Fig. 8c, Fig. 10a and Fig. 12b show that both small and large grains were randomly distributed in the area near or far away from the particles. It is difficult to determine the effect of the particles (such as PSN) on the micromechanisms of DGG by these metallographs. However, we can understand the dependence of grain size on hot working parameters by using the statistical data from metallographs.

(3) Temperature range of 440-500 ºC (η = 22-49, AGG)

When the temperature increased above 440 ºC, AGG took place instantly as illustrated in section 3.5.1. In terms of a rigorous definition, the AGG in the complete recrystallization system is also known as a subsequent process of the primary recrystallization.

(4) Temperature of 450 ºC, equicohesive point (T_{eq})

The early concept of equicohesive temperature was proposed by Rosenhain et al. [65]. Below the equicohesive temperature the grain boundary is presumed to be strong, whereas above this temperature the grain boundary is presumed to be weak. At lower temperatures, plastic deformation generally occurs in a manner of slip within the crystallite interior, whereas above T_{eq} the grain boundaries would contribute to partial plastic deformation by grain boundary sliding, especially at lower strain rates. As

shown in Fig. 14a, after the deformation at 460 ºC and 0.01 s^{-1}, there exists a noticeable wedge crack near the edge of the transverse cross-section. Fig. 14b illustrates the view field location of the specimen transverse section. Because the region denoted in Fig. 14b was subjected to the tensile stress during hot compression, the defects such as debonding, voids and cracks would be easily to find.

If the SiC particles are not situated just on the grain boundary for an effective pinning, the grain boundary sliding readily occurs at the temperatures above equicohesive point. On the other hand, when the grains grow to a certain degree the boundaries will not migrate further. As a consequence, under lower strain rates the grain boundary sliding occurs between the specific large grains subjected to tensile stress, and causes the formation of wedge crack or intergranular cavitation at the grain boundary triple junction with stress concentration. Considering the trend change of η versus temperature curves (Fig. 11) and the prominent microstructure features in the deformed specimens, the temperature of 450 ºC (~0.8 T_m) can be defined as the equicohesive point.

3.5.3 Abnormal evolution of microstructure corresponding to η curve

In Fig.11, the η curve of 0.1 s^{-1} ascends monotonically around the temperature 460 ºC and the η value is higher than that for the other curves. This difference results from the nonuniform microstructure evolution. Fig. 15a shows the overall morphology in the longitudinal cross-section of the specimen compressed at 460 ºC and 0.1 s^{-1}. The bottom half of specimen exhibits the large grains after AGG, whereas the upper half is of the fine-grained microstructure after DGG as shown in Fig. 15b. From the results

above, at 460 ºC uniform AGG occurred under the strain rate of 0.01 s^{-1} (Fig. 8a) and 1 s^{-1} (Fig. 10b), which is lower and higher than 0.1 s^{-1}, respectively.

For the nonuniform structure under cold rolling and static annealing condition, it might be interpreted that the regions where recrystallization occurs more rapidly are those with larger stored energy and a larger number of the higher angle grain boundaries required for initiating recrystallization [66]. In the view of system energy, AGG originated on the half side of specimen is probably in favor of a dynamic equilibrium between the stored energy in the system interior and the total power applied for plastic deformation. The parameter of 460 ºC and 0.1 s^{-1} just approaches to this critical condition for inhomogeneous microstructure formation. Therefore, this parameter should be avoided during hot working.

3.6 Damage analysis

The specimens after compressed to a true strain of 0.9 under different deformation conditions are shown in Fig. 16. It is readily noted that the damage level of cracks aggravates with the increasing temperature and strain rate. As the temperature exceeds the T_{eq}, grain boundary sliding makes an increasing contribution to plastic deformation. This grain boundary diffusion controlled sliding is a time-dependent process. At lower strain rates, the plastic deformation can be accommodated by an adequate diffusion. However, at higher strain rates, the stress concentration tends to occur at the grain boundaries and matrix/particle interfaces in which the defects such as micro-pores or micro-cracks are likely to arise. At 495 ºC, cracking occurred on the lateral surface of all the specimens, and the cracks enlarged as the strain rate increased.

At 460 ºC, no apparent macrocracks could be found in the strain rate range of 0.001-1 s^{-1}. Under temperatures of 425 ºC and below, all specimens exhibited the smooth surface without cracks.

Fig. 17 shows the internal damage of specimens, and the view fields are the transverse cross-section as illustrated in Fig. 14b. In this plane the zone near the edge is subjected to tensile stress.

At 425 ºC, any forms of internal damage could not be found even under the high strain rate 1 s^{-1}, as shown in Fig. 17a.

When the temperature rose up to 460 ºC, the macroscopic cracks did not generate on the lateral surface at each strain rate, as seen in Fig. 16. However, under a low strain rate of 0.001 s^{-1}, a number of cavities and cracks were generated in the regions far from and near the edge (Fig. 17b). In Fig. 17c, not only the interface debonding but also the initial cracks of about 20-30 μm were generated in the vicinity of the edge. Even in the site with a distance of 2.2 mm from the edge (the radius of the transverse observation section ~6.7 mm) debonding still took place around a few of particles denoted by the arrows in Fig. 17d.

During deformation of composites, the SiC particles experience elastic deformation while the matrix experience plastic deformation. For this situation the local deformation gradients are accommodated by the geometrically-necessary dislocations which are stored near the particle-matrix interface [67]. At elevated temperatures, the strength of interface reduces more rapidly than that of SiC reinforcement, and also with the increasing of strain rate the relaxation of interfacial stresses by lattice cannot

effectively carry out. In this case, the deformation incompatibility will be accommodated by the cavities generated at the interface. Thus, the debonding takes place subsequently with the gathering of cavities.

During hot compression, in the middle transverse plane the tensile strain in the interior was smaller than that near the edge. Considering the above observations, it could be suggested that under tension state the damage in the composites generally performed as interface debonding before the occurrence of crack propagation.

At the high temperature of 495 ºC, even though there were little macroscopic cracks under the strain rate of 0.001 s^{-1} (Fig. 16), many large voids or cracks about 50-100 μm in size appeared in the interior near the edge, as shown in Fig. 17e. When the strain rate reached 0.01 s^{-1}, those discontinuous small voids and cracks merged to form the extended cracks. The damages as shown in Fig. 17f became more serious.

By comparing Fig. 4b with Fig. 16, it is noted that there exists an excellent coincident correlation between the plotted instability region from MDMM and the external crack morphology of compressed samples. For the fine-grained SiCp/2014Al composite fabricated by cast-plus-extruded route, the high temperatures and strain rates of around 495 ºC (0.85 T_m) and 1 s^{-1} are unsafe hot working parameters, under which the various forms of damages as mentioned above are very susceptible to generate in the area subjected to tensile stress. In the previous studies [10, 16, 19, 68, 69], it was commonly suggested that at lower temperatures and higher strain rates, void formation occurred at hard particles. That is not in agreement with the observations in this work.

4. Conclusions

In the study, a novel compression data analysis method was developed for enchancing accuracy of processing map. Futhermore, the strain rate sensitivity map, temperature sensitivity map and processing map were combined to present a thorough regularity for microstructure evolution. For the selected 14vol.%SiCp/2014Al composite, the three maps achieved good consistancy in description for deformation behaviors. The study has presented a reliable prediction of deformation mechanisms. The following conclusions can be drawn:

(1) The strain rate sensitivity map indicated that temperature generally has a more significant effect on the deformation mechanism than strain rate. From temperature sensitivity map, an AGG transition point was ascertained to be 440 ºC. The composite should be processed at temperatures under the AGG point.

(2) Different deformation mechanisms were determined under various temperature ranges: i. DRV was the dominant deformation mode at 350-400 ºC; ii. DRX occurred in manner of DGG at 400-440 ºC; iii. AGG operated above 440 ºC; iv. 450 ºC (0.8 T_m) corresponded to the equicohesive point (T_{eq}).

(3) The instability map based on the MDMM exhibited a well coincident correlation with the external crack of overall samples. For 14 vol.% SiCp/2014Al composites, the cracking more readily occurred at the high temperature and strain rate (495 ºC/1 s^{-1}). This and the adjacent parameters must be avoided during hot deformation process.

Acknowledgements

The authors gratefully acknowledge the support of National Natural Science Foundation of China under grant No. U1508216 and National Basic Program of China under grant No. 2012CB619600. The authors also thank Prof. Q. B. Ouyang, Shanghai Jiao Tong University, for providing the samples of 14 vol.% SiCp/2014Al composite, and Prof. X. X. Zhang, Harbin Institute of Technology, for offering the TEM experiments.

References

[1] S.P. Rawal, Metal-matrix composites for space applications, JOM, 53 (2001) 14-17.

[2] D.B. Miracle, Metal matrix composites – From science to technological significance, Composites Science and Technology, 65 (2005) 2526-2540.

[3] K.U. Kainer, Basics of Metal Matrix Composites, in: Metal Matrix Composites, Wiley-VCH Verlag GmbH & Co. KGaA, 2006, pp. 1-54.

[4] I. Akkurt, K. Günoğlu, A. Çalik, M.S. Karakas, Determination of gamma ray attenuation coefficients of Al-4% Cu/B4C metal matrix composites at 662, 1173 and 1332 keV, Bulletin of Materials Science, 37 (2014) 1175-1179.

[5] A.P. Divecha, S.G. Fishman, S.D. Karmarkar, Silicon Carbide Reinforced Aluminum – A Formable Composite, JOM, 33 (1981) 12-17.

[6] W.L. Zhang, J.X. Wang, F. Yang, Z.Q. Sun, M.Y. Gu, Recrystallization Kinetics of Cold-rolled Squeeze-cast Al/SiC/15w Composites, Journal of Composite Materials, 40 (2006) 1117-1131.

[7] M. Jahedi, B. Mani, S. Shakoorian, E. Pourkhorshid, M.H. Paydar, Deformation rate effect on the microstructure and mechanical properties of Al–SiCp composites consolidated by hot extrusion, Materials Science and Engineering: A, 556 (2012) 23-30.

[8] M. Stonis, T. Rüther, B.-A. Behrens, Analysis of Material Characteristics and

Forging Parameters for Flashless Forged Aluminum-Matrix Composites, Materials and Manufacturing Processes, 29 (2014) 140-145.

[9] Y.V.R.K. Prasad, H.L. Gegel, S.M. Doraivelu, J.C. Malas, J.T. Morgan, K.A. Lark, D.R. Barker, Modeling of dynamic material behavior in hot deformation: forging of Ti-6242, Metallurgical Transactions A, 15 (1984) 1883-1892.

[10] B.V. Radhakrishna Bhat, Y.R. Mahajan, H.M. Roshan, Y.V.R.K. Prasad, Characteristics of superplasticity domain in the processing map for hot working of an Al alloy 2014-20vol.%Al2O3 metal matrix composite, Materials Science and Engineering: A, 189 (1994) 137-145.

[11] B.V. Radhakrishna Bhat, Y.R. Mahajan, H.M. Roshan, Y.V.R.K. Prasad, Processing map for hot working of 6061 Al–10 vol.-%Al2O3 metal matrix composite, Materials Science and Technology, 11 (1995) 167-173.

[12] S.V.S.N. Murty, B.N. Rao, Instability map for hot working of 6061 Al-10 vol% Al2O3 metal matrix composite, Journal of Physics D: Applied Physics, 31 (1998) 3306-3311.

[13] S.V.S.N. Murty, B.N. Rao, B.P. Kashyap, On the hot working characteristics of 6061Al-SiC and 6061-Al2O3 particulate reinforced metal matrix composites, Composites Science and Technology, 63 (2003) 119-135.

[14] P. Cavaliere, E. Cerri, P. Leo, Hot deformation and processing maps of a particulate reinforced 2618/Al2O3/20p metal matrix composite, Composites Science and Technology, 64 (2004) 1287-1291.

[15] P. Cavaliere, E. Evangelista, Isothermal forging of metal matrix composites: Recrystallization behaviour by means of deformation efficiency, Composites Science and Technology, 66 (2006) 357-362.

[16] P. Zhang, F.G. Li, Q. Wan, Constitutive equation and processing map for hot deformation of SiC particles reinforced metal matrix composites, Journal of materials engineering and performance, 19 (2010) 1290-1297.

[17] M. Rajamuthamilselvan, S. Ramanathan, Development of Processing Map for 7075 Al/20% SiCp Composite, Journal of Materials Engineering and Performance, 21 (2012) 191-196.

[18] S.V.S.N. Murty, M.S. Sarma, B.N. Rao, On the evaluation of efficiency parameters in processing maps, Metallurgical and Materials Transactions A, 28 (1997) 1581-1582.

[19] S.V.S.N. Murty, B.N. Rao, B.P. Kashyap, Instability criteria for hot deformation of materials, International Materials Reviews, 45 (2000) 15-26.

[20] K.-k. Deng, J.-c. Li, F.-j. Xu, K.-b. Nie, W. Liang, Hot deformation behavior and processing maps of fine-grained SiCp/AZ91 composite, Materials & Design, 67 (2015) 72-81.

[21] H. Rastegari, A. Kermanpur, A. Najafizadeh, D. Porter, M. Somani, Warm deformation processing maps for the plain eutectoid steels, Journal of Alloys and Compounds, 626 (2015) 136-144.

[22] D.-X. Wen, Y.C. Lin, J. Chen, J. Deng, X.-M. Chen, J.-L. Zhang, M. He, Effects of initial aging time on processing map and microstructures of a nickel-based superalloy, Materials Science and Engineering: A, 620 (2015) 319-332.

[23] S. Gangolu, A. Gourav Rao, I. Sabirov, B.P. Kashyap, N. Prabhu, V.P. Deshmukh, Development of constitutive relationship and processing map for Al-6.65Si-0.44Mg alloy and its composite with B4C particulates, Materials Science and Engineering: A, 655 (2016) 256-264.

[24] X. Li, C. Liu, X. Sun, M. Ma, R. Liu, Hot deformation behaviour and processing maps of AA6061-10 vol.% SiC composite prepared by spark plasma sintering, Science China Technological Sciences, 59 (2016) 980-988.

[25] S. Samal, M.R. Rahul, R.S. Kottada, G. Phanikumar, Hot deformation behaviour and processing map of Co-Cu-Fe-Ni-Ti eutectic high entropy alloy, Materials Science and Engineering: A, 664 (2016) 227-235.

[26] T. Wang, K. Nie, K. Deng, W. Liang, Analysis of hot deformation behavior and microstructure evolution of as-cast SiC nanoparticles reinforced magnesium matrix composite, Journal of Materials Research, 31 (2016) 3437-3447.

[27] G.-z. Quan, L. Zhang, X. Wang, Y.-l. Li, Correspondence between microstructural evolution mechanisms and hot processing parameters for Ti-13Nb-13Zr biomedical alloy in comprehensive processing maps, Journal of Alloys

and Compounds, 698 (2017) 178-193.

[28] H.L. Gegel, J.C. Malas, S.M. Doraivelu, V. Shende, Modeling techniques used in forging process design, ASM Handbook, 14 (1988) 417-438.

[29] J.M. Alexander, Mapping dynamic material behaviour, in: Modelling Hot Deformation of Steels, Springer, 1989, pp. 101-115.

[30] J.C. Malas, Methodology for design and control of thermomechanical processes, in, Ohio University, Ann Arbor, 1991, pp. 33-45.

[31] Y.V.R.K. Prasad, T. Seshacharyulu, Modelling of hot deformation for microstructural control, International Materials Reviews, 43 (1998) 243-258.

[32] Y.V.R.K. Prasad, Author's reply: Dynamic materials model: Basis and principles, Metallurgical and Materials Transactions A, 27 (1996) 235-236.

[33] R. Liu, W. Cao, T. Fan, C. Zhang, D. Zhang, Development of processing maps for 3 vol.% TiCp/AZ91D composites material, Materials Science and Engineering: A, 527 (2010) 4687-4693.

[34] S.S. Zhou, K.K. Deng, J.C. Li, K.B. Nie, F.J. Xu, H.F. Zhou, J.F. Fan, Hot deformation behavior and workability characteristics of bimodal size SiCp/AZ91 magnesium matrix composite with processing map, Materials & Design, 64 (2014) 177-184.

[35] T. Feng, X. Chen, L. Wu, S. Lou, Diffusion welding of SiCp/2014Al composites using Ni as interlayer, Journal of University of Science and Technology Beijing, 13 (2006) 267-271.

[36] Y.S.Su,Q.B. Ouyang,W.L. Zhang,Z.Q. Li, Q. Guo, G.L. Fan, D. Zhang, Composite structure modeling and mechanical behavior of particle reinforced metal matrix composites, Materials Science and Engineering A, 597 (2014) 359-369.

[37] A. Gholinia, F.J. Humphreys, P.B. Prangnell, Production of ultra-fine grain microstructures in Al–Mg alloys by coventional rolling, Acta Materialia, 50 (2002) 4461-4476.

[38] S. Gourdet, F. Montheillet, Effects of dynamic grain boundary migration during the hot compression of high stacking fault energy metals, Acta Materialia, 50 (2002) 2801-2812.

[39] D. Feng, X.M. Zhang, S.D. Liu, Y.L. Deng, Constitutive equation and hot deformation behavior of homogenized Al–7.68Zn–2.12Mg–1.98Cu–0.12Zr alloy during compression at elevated temperature, Materials Science and Engineering: A, 608 (2014) 63-72.

[40] D. Webster, Effect of lithium on the mechanical properties and microstructure of SiC whisker reinforced aluminum alloys, Metallurgical Transactions A, 13 (1982) 1511-1519.

[41] R.S. Mishra, A.B. Pandey, Some observations on the high-temperature creep behavior of 6061 Al-SiC composites, Metallurgical Transactions A, 21 (1990) 2089.

[42] K.-T. Park, E.J. Lavernia, F.A. Mohamed, High temperature creep of silicon carbide particulate reinforced aluminum, Acta Metallurgica et Materialia, 38 (1990) 2149-2159.

[43] K.-T. Park, F.A. Mohamed, Creep strengthening in a discontinuous SiC-Al composite, Metallurgical and Materials Transactions A, 26 (1995) 3119-3129.

[44] Z.G. Lin, F.A. Mohamed, Creep and microstructure in powder metallurgy 15 vol.% SiCp-2009 Al composite, Journal of Materials Science, 47 (2012) 2975-2984.

[45] A.K.S.K. Kumar, Criteria for predicting metallurgical instabilities in processing maps, in, Indian Institute of Science, Bangalore, India, 1987.

[46] J.K. Chakravartty, Y.V.R.K. Prasad, M.K. Asundi, Processing map for hot working of alpha-zirconium, Metallurgical Transactions A, 22 (1991) 829-836.

[47] H. Ziegler, I.N. Sneddon, R. Hill, Progress in solid mechanics, John Wiley & Sons, New York 1963.

[48] H. Mirzadeh, A. Najafizadeh, M. Moazeny, Flow curve analysis of 17-4 PH stainless steel under hot compression test, Metallurgical and Materials Transactions A, 40 (2009) 2950-2958.

[49] G.L. Ji, F.G. Li, Q.H. Li, H.Q. Li, Z. Li, A comparative study on Arrhenius-type constitutive model and artificial neural network model to predict high-temperature deformation behaviour in Aermet100 steel, Materials Science and Engineering: A, 528 (2011) 4774-4782.

[50] Y.C. Lin, D.X. Wen, J. Deng, G. Liu, J. Chen, Constitutive models for

high-temperature flow behaviors of a Ni-based superalloy, Materials & Design, 59 (2014) 115-123.

[51] H. Mirzadeh, A simplified approach for developing constitutive equations for modeling and prediction of hot deformation flow stress, Metallurgical and Materials Transactions A, 46 (2015) 4027-4037.

[52] B.L. Xiao, J.Z. Fan, X.F. Tian, W.Y. Zhang, L.K. Shi, Hot deformation and processing map of 15%SiCp/2009 Al composite, Journal of Materials Science, 40 (2005) 5757-5762.

[53] J.C. Shao, B.L. Xiao, Q.Z. Wang, Z.Y. Ma, Y. Liu, K. Yang, Constitutive flow behavior and hot workability of powder metallurgy processed 20 vol.%SiCp/2024Al composite, Materials Science and Engineering: A, 527 (2010) 7865-7872.

[54] C.X. Wang, F.X. Yu, D.Z. Zhao, X. Zhao, L. Zuo, Hot deformation and processing maps of DC cast Al-15%Si alloy, Materials Science and Engineering: A, 577 (2013) 73-80.

[55] J. Zhang, H. Di, H. Wang, K. Mao, T. Ma, Y. Cao, Hot deformation behavior of Ti-15-3 titanium alloy: a study using processing maps, activation energy map, and Zener-Hollomon parameter map, Journal of Materials Science, 47 (2012) 4000-4011.

[56] J. Zhang, H. Di, K. Mao, X. Wang, Z. Han, T. Ma, Processing maps for hot deformation of a high-Mn TWIP steel: A comparative study of various criteria based on dynamic materials model, Materials Science and Engineering: A, 587 (2013) 110-122.

[57] H. Watanabe, T. Mukai, K. Higashi, Influence of temperature and grain size on threshold stress for superplastic flow in a fine-grained magnesium alloy, Metallurgical and Materials Transactions A, 39 (2008) 2351-2362.

[58] K.B. Hyde, P.S. Bate, Dynamic grain growth in Al–6Ni: Modelling and experiments, Acta Materialia, 53 (2005) 4313-4321.

[59] O.V. Rofman, P.S. Bate, I. Brough, F.J. Humphreys, Study of dynamic grain growth by electron microscopy and EBSD, Journal of Microscopy, 233 (2009) 432-441.

[60] Z. Li, A.M. Samuel, F.H. Samuel, C. Ravindran, S. Valtierra, Effect of alloying

elements on the segregation and dissolution of CuAl2 phase in Al-Si-Cu 319 alloys, Journal of Materials Science, 38 (2003) 1203-1218.

[61] M. Rajamuthamilselvan, S. Ramanathan, Hot-working behavior of 7075 Al/15% SiCp composites, Materials and Manufacturing Processes, 27 (2012) 260-266.

[62] S.F. Exell, D.H. Warrington, Sub-grain boundary migration in aluminium, Philosophical Magazine, 26 (1972) 1121-1136.

[63] F.J. Humphreys, The nucleation of recrystallization at second phase particles in deformed aluminium, Acta Metallurgica, 25 (1977) 1323-1344.

[64] F.J. Humphreys, W.S. Miller, M.R. Djazeb, Microstructural development during thermomechanical processing of particulate metal-matrix composites, Materials Science and Technology, 6 (1990) 1157-1166.

[65] A.H. Chokshi, A. Rosen, J. Karch, H. Gleiter, On the validity of the hall-petch relationship in nanocrystalline materials, Scripta Metallurgica, 23 (1989) 1679-1683.

[66] M. Somerday, F.J. Humphreys, Recrystallisation behaviour of supersaturated Al–Mn alloys Part 1 – Al–1.3 wt-%Mn, Materials Science and Technology, 19 (2003) 20-29.

[67] M.F. Ashby, The deformation of plastically non-homogeneous materials, Philosophical Magazine, 21 (1970) 399-424.

[68] G. Ganesan, K. Raghukandan, R. Karthikeyan, B. Pai, Development of processing maps for 6061 Al/15% SiCp composite material, Materials Science and Engineering: A, 369 (2004) 230-235.

[69] Y.V.R.K. Prasad, K.P. Rao, S. Sasidhar, Hot working guide: a compendium of processing maps, ASM international, 2015.

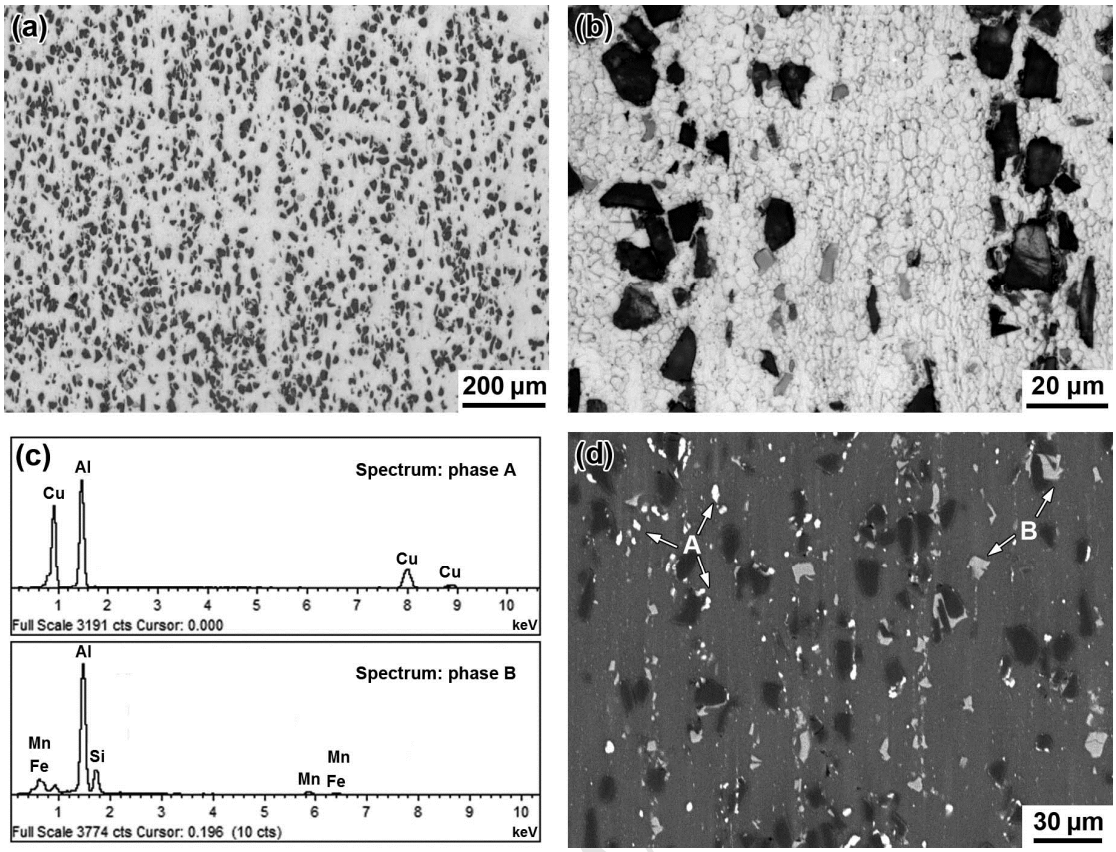

Fig. 1 Initial microstructures of as-received cast-plus-extruded 14 vol.% SiCp/2014Al composite: (a) SiCp distribution, (b) grain configuration of matrix alloy, (c) SEM/EDS of precipitated phases, (d) SEM backs-scattered electron image (Extrusion direction is vertical to the horizontal.)

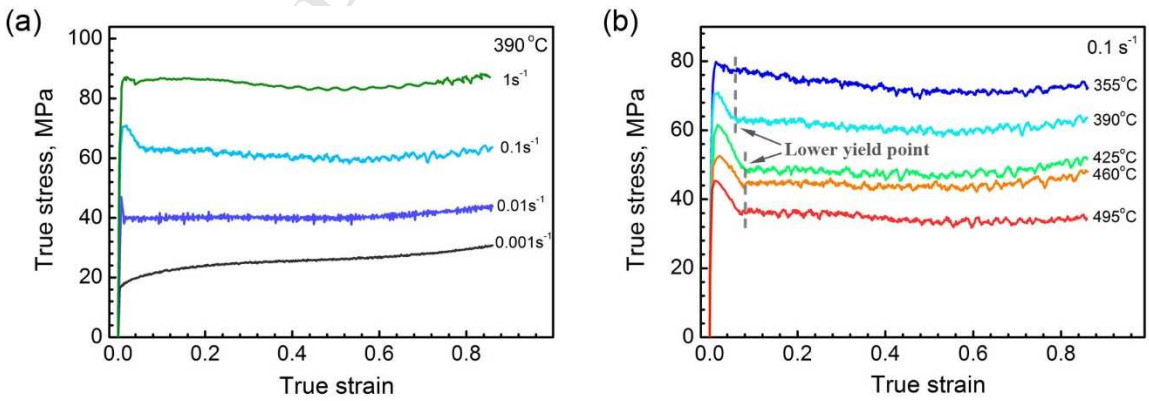

Fig. 2 True stress vs. true strain curves of 14 vol.% SiCp/2014Al composites at (a) 390 ºC for varying strain rates, (b) strain rate 0.1 s^{-1} for varying temperatures

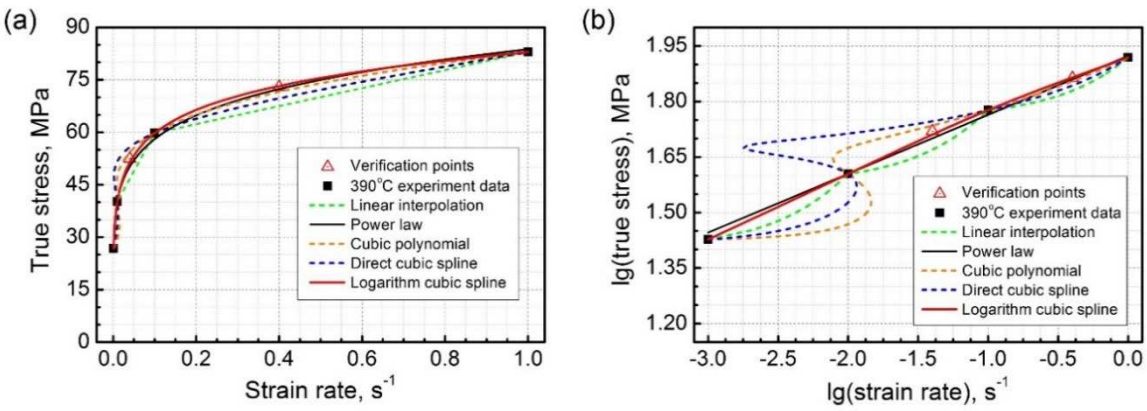

Fig. 3 The curves fitted by different methods for 14 vol.% SiCp/2014Al composite at true strain 0.6: (a) true stress vs. strain rate, (b) lg(true stress) vs. lg(strain rate)

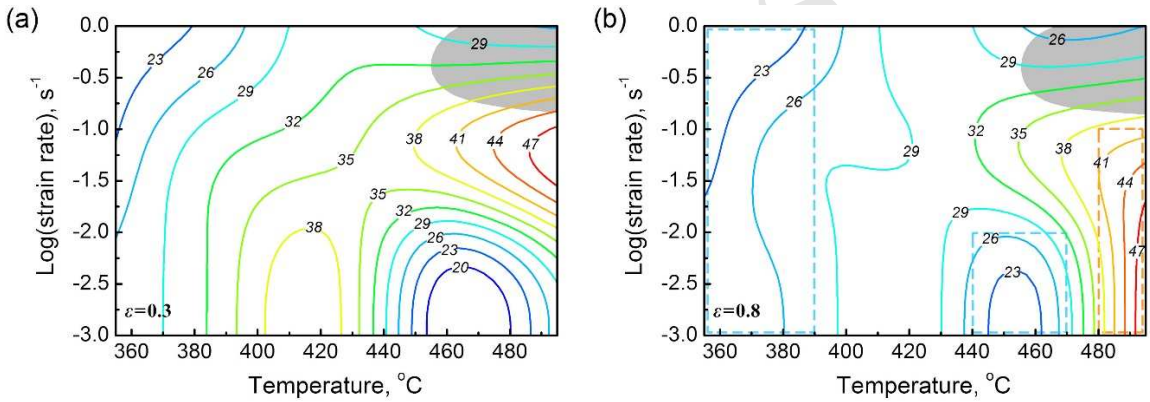

Fig. 4 The processing map (power dissipation efficiency, η, %) of 14 vol.% SiCp/2014Al composite (a) true strain 0.3, (b) true strain 0.8

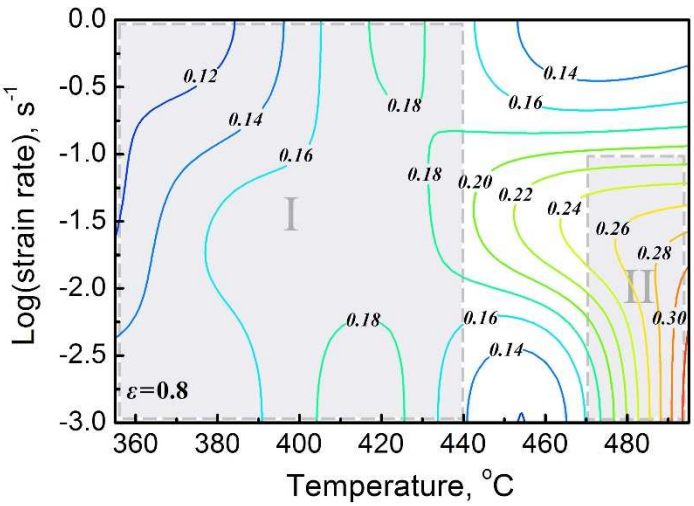

Fig. 5 The strain rate sensitivity, *m*, contour map of 14 vol.% SiCp/2014Al composite

at true strain 0.8

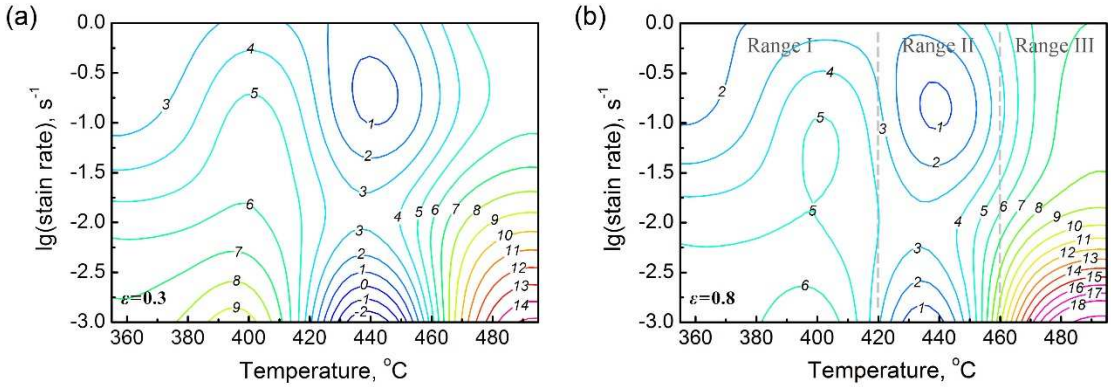

Fig. 6 The temperature sensitivity, *s*, contour map of 14 vol.% SiCp/2014Al composite: (a) true strain 0.3, (b) true strain 0.8

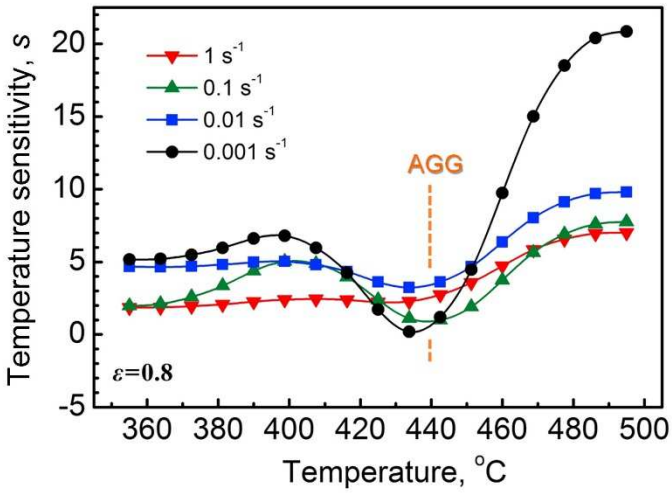

Fig. 7 The variation of temperature sensitivity, *s*, value curves with temperature under various strain rates at true strain 0.8 for 14 vol.% SiCp/2014Al composite

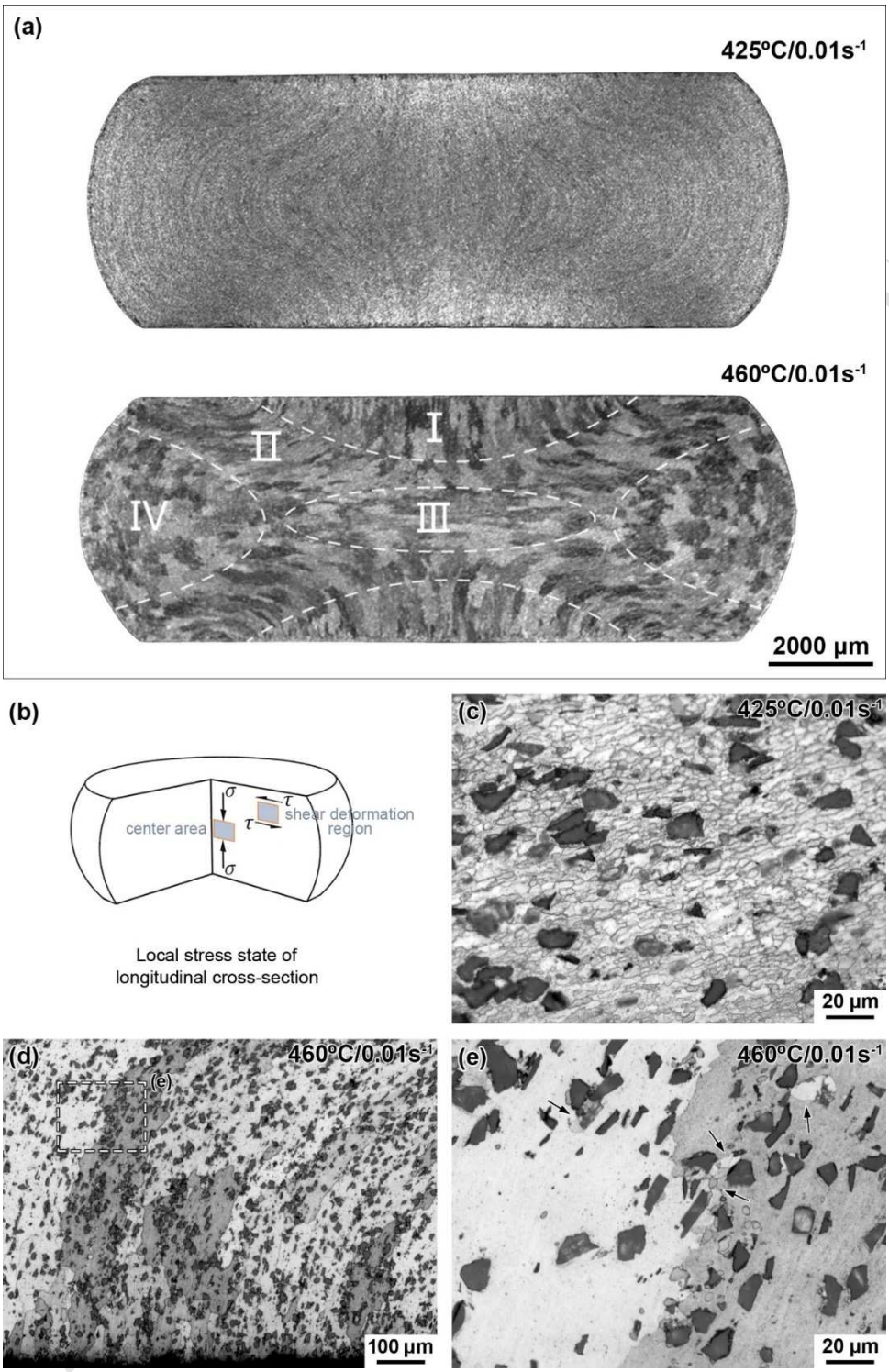

Fig. 8 Microstructures of the specimens tested at strain rate of 0.01 s^{-1} with true strain of 0.9: (a) macrograph of longitudinal cross-section at 425 and 460 ºC, (b) view fields location of longitudinal section (c) shear deformation region at 425 ºC, (d) shear deformation region at 460 ºC, (e) local region in the dotted box of (d)

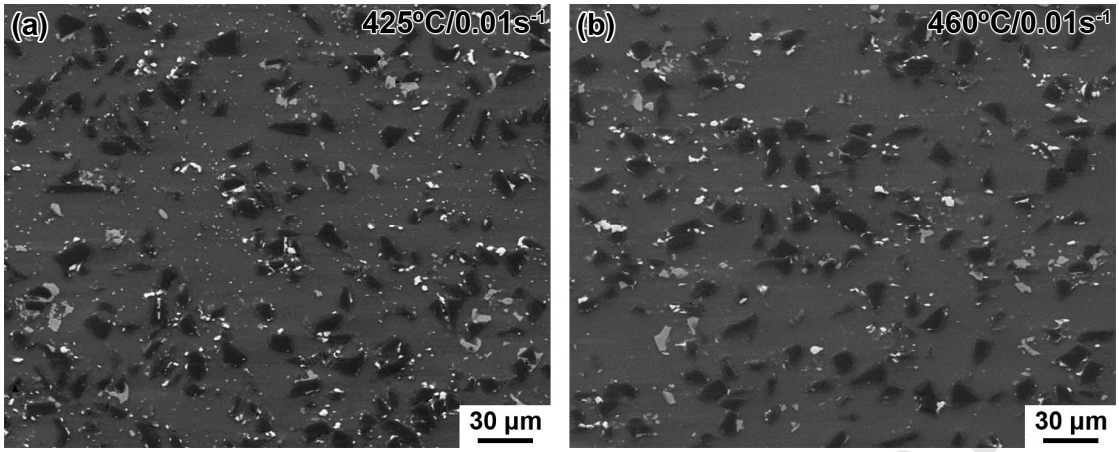

Fig. 9 SEM backs-scattered electron images of the specimens tested at strain rate of 0.01 s^{-1} with true strain of 0.9: (a) 425 ºC, (b) 460 ºC

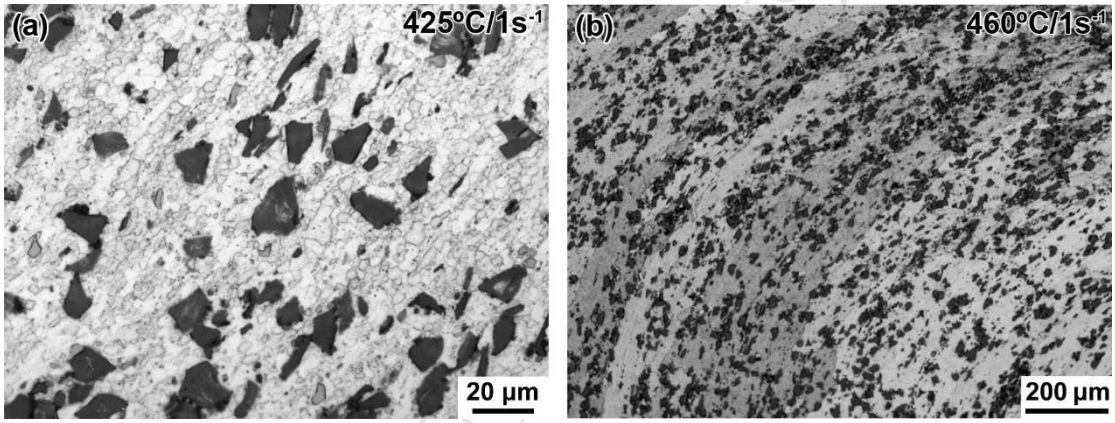

Fig. 10 Microstructures of specimens tested under strain rate of 1 s^{-1} with true strain of 0.9 at (a) 425 ºC and (b) 460 ºC

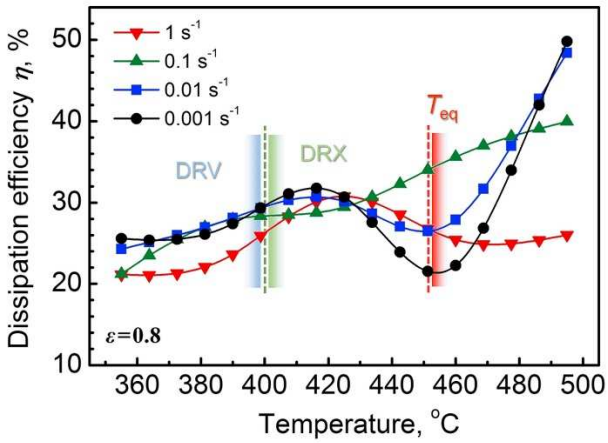

Fig. 11 The variation of η value (%) with temperature under various strain rates at true strain of 0.8 for 14 vol.% SiCp/2014Al composite

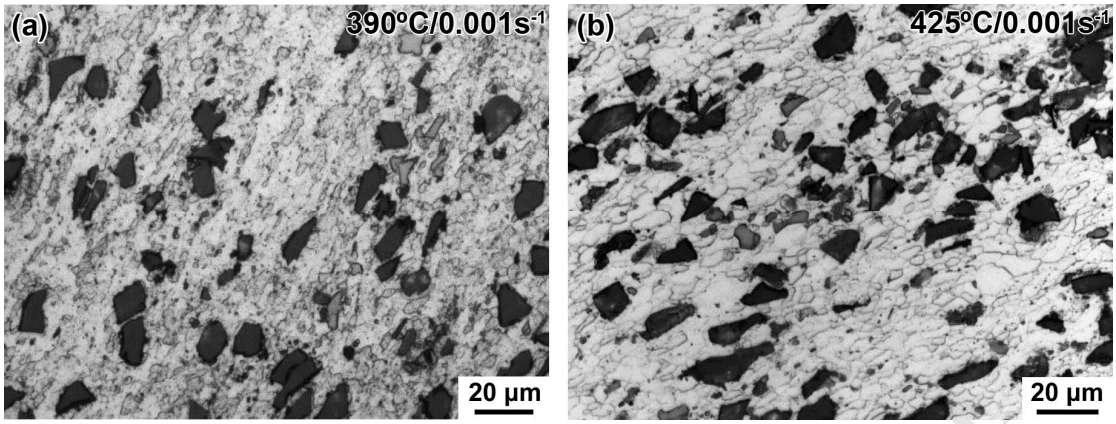

Fig. 12 Microstructures in the shear deformation zone tested under strain rate of 0.001 s^{-1} with true strain of 0.9 at (a) 390 ºC and (b) 425 ºC

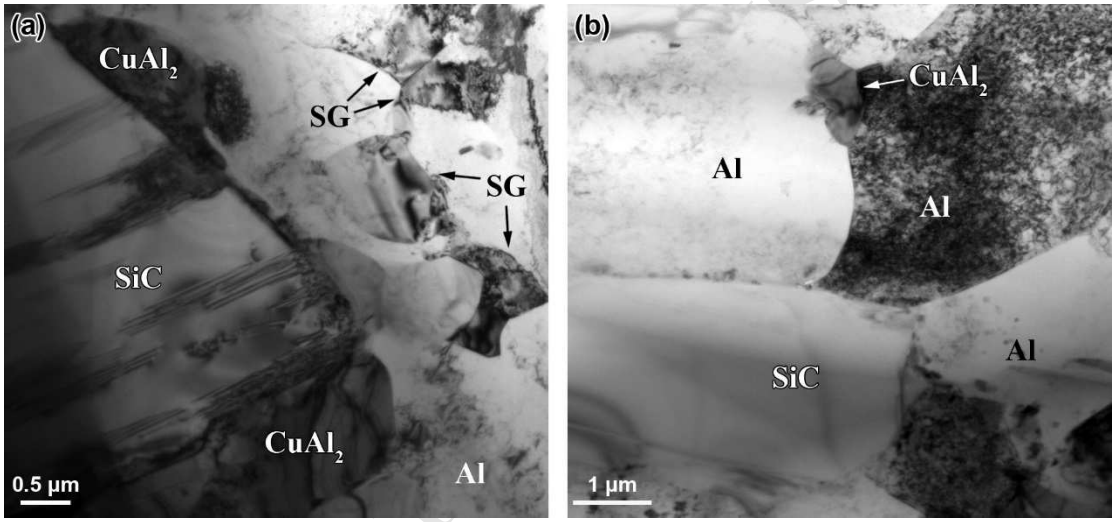

Fig. 13 TEM images of the specimens compressed with true strain of 0.9 at: (a) 355 ºC/1 s^{-1}, (b) 425 ºC/1 s^{-1}

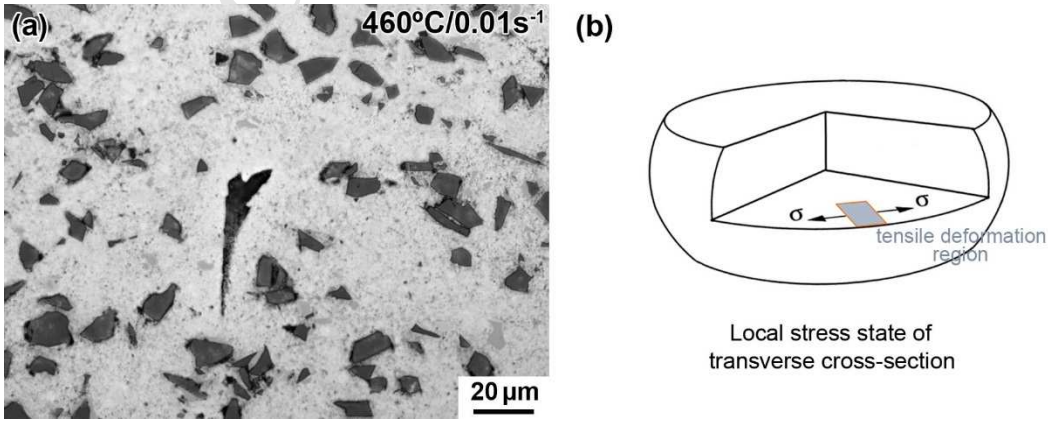

Fig. 14 Internal damage observation of the specimen compressed at 460 ºC/0.01 s^{-1} to

true strain of 0.9: (a) wedge crack near the edge on the transverse section, (b) the view field location of transverse cross-section

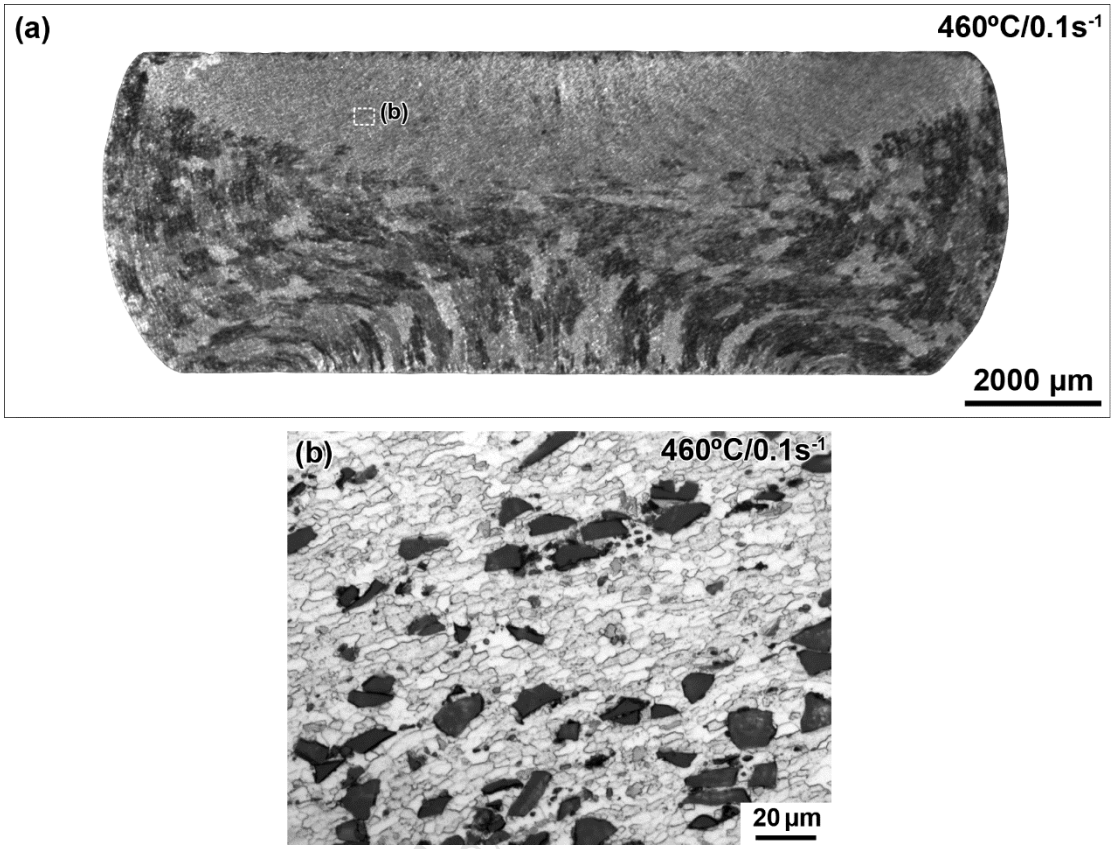

Fig. 15 Microstructures of the specimen compressed at 460 ºC/0.1 s^{-1} to true strain of 0.9: (a) overall grains distribution in the longitudinal cross-section, (b) signified view of grain structure in the shear deformation region as shown by rectangle b in Fig. 13a

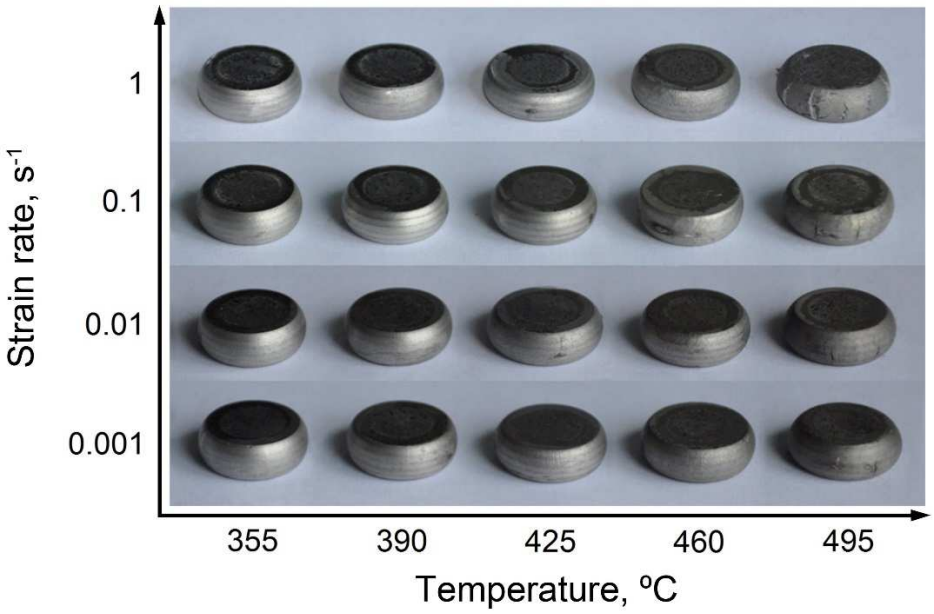

Fig. 16 External crack morphologies of all compressed samples at true strain of 0.9

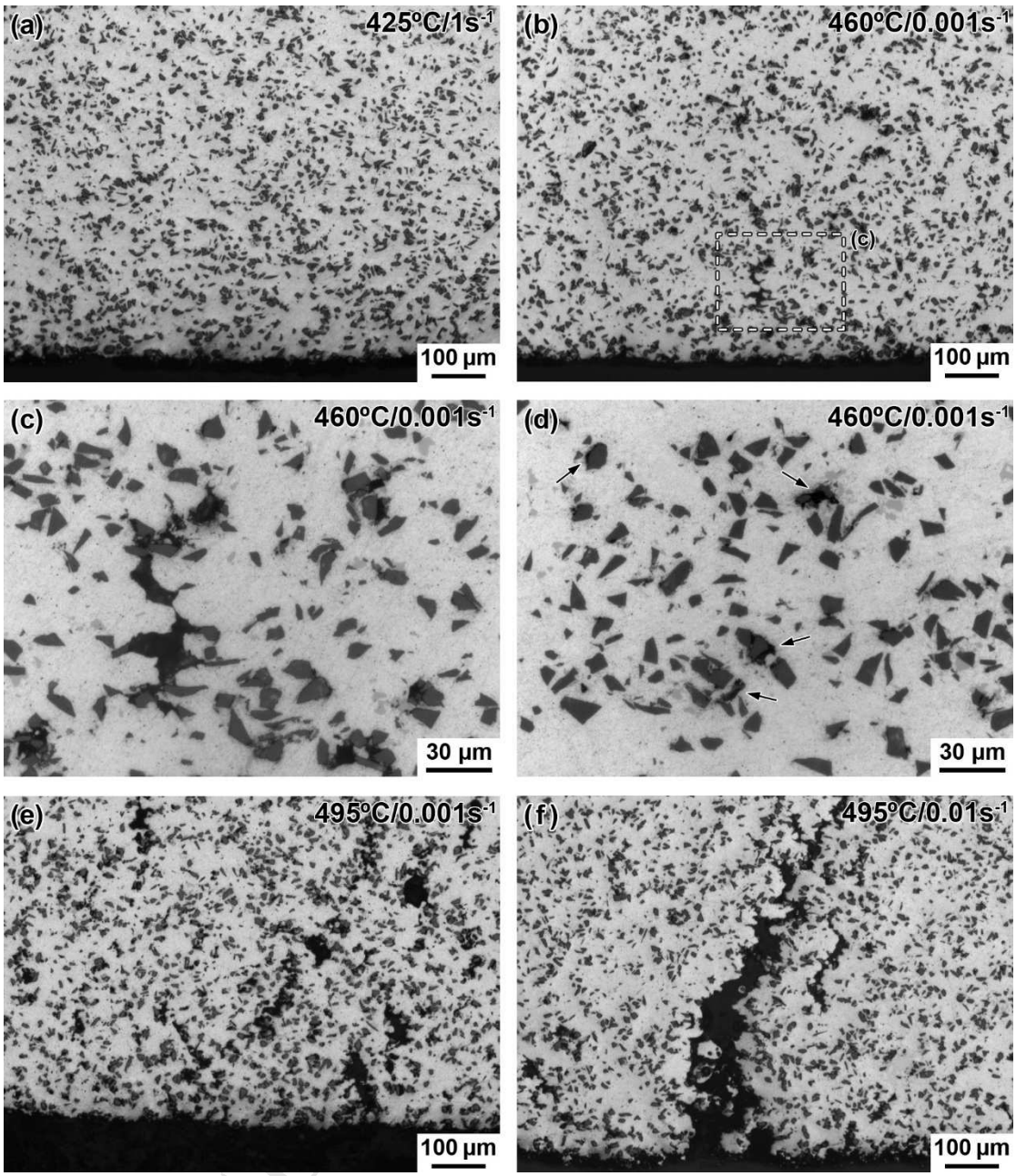

Fig. 17 Internal damage state in transverse cross-section of specimens compressed to true strain of 0.9: (a) at 425 ºC/1 s^{-1}, (b) at 460 ºC/0.001 s^{-1}, (c) local region in the dotted box of (b), (d) at the area far away from edge at 460 ºC/0.001 s^{-1}, (e) at 495 ºC/0.001 s^{-1}, (f) at 495 ºC/0.01 s^{-1}

Highlights

• Hot deformation behaviors of SiCp/2014Al composite were investigated.

• Temperature, strain rate sensitivity maps and processing map are in good consistency.

• Transition temperatures of deformation mechanisms were predicted accuratley.

• Crack forming conditions agree well with instability region of processing map.